Quasiperiodic Moiré Plasmonic Crystals

Steven M. Lubin,[†] Alexander J. Hryn,[‡] Mark D. Huntington,[‡] Clifford J. Engel,[†] and Teri W. Odom[†,‡,*]

[†]Department of Chemistry, [‡]Department of Materials Science & Engineering, Northwestern University, Evanston, Illinois 60208, United States

ABSTRACT This paper describes the properties of silver plasmonic crystals with quasiperiodic rotational symmetries. Compared to periodic plasmonic crystals, quasiperiodic moiré structures exhibited an increased number of surface plasmon polariton modes, especially at high angles of excitation. In addition, plasmonic band gaps were often formed at the intersections of these new modes. To identify the origin and predict the location of the band gaps, we developed a Bragg-based indexing system using the reciprocal lattice vectors of the moiré plasmonic crystals. We showed that even more complicated quasiperiodic geometries could also be described by this indexing model. We anticipate that these quasiperiodic lattices will be useful for applications that require the concentration and manipulation of light over a broadband spectrum.

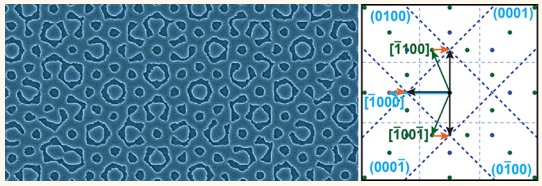

KEYWORDS: surface plasmon polaritons · quasiperiodic · moiré patterns · high rotational symmetry lattices · plasmonic band gaps · angle-resolved reflectance spectroscopy · pseudo-Brillouin zones

Light can be concentrated below the diffraction limit as surface plasmon polaritons (SPPs),[1] electromagnetic excitations formed from the coupling of light and conduction band electrons at a metal-dielectric interface.[2,3] One method to excite SPPs using free-space light is to structure the surface of a metal film with subwavelength patterns; periodic 1D and 2D arrays are typically referred to as plasmonic crystals (PCs).[2−5] The SPP resonances of PCs can be controlled by the geometry of the patterns as well as the properties of the metal and dielectric materials.[3,6] The tunability of the resonances, their energies, and their band gaps has enabled PCs to impact a range of applications, from biosensing[7,8] to far-field focusing of light.[9,10] Since the number and range of SPP modes are mostly limited by periodicity, other potential applications have largely been precluded, such as plasmonic photovoltaics, where broadband light trapping and waveguide effects are desired.[11] One method to produce a broadband spectrum is the creation of plasmonic superlattices with periodicities over multiple length scales.[12] Another strategy is to reduce the symmetry of the PC in order to lift degeneracies among SPP modes.[13] Conversely, increasing rotational symmetry can increase the number of SPPs. Periodic arrays in 2D lattices are limited, however, to a maximum of 6-fold symmetry because of the crystallographic restriction theorem.[14] As a result, geometries that have nontraditional periodic arrangements can be considered as the basis for new PC architectures.

Quasiperiodic lattices are nonperiodic structures that contain translational order but lack translational symmetry.[15] These arrays can exceed the 6-fold symmetry restriction in two dimensions. For instance, quasiperiodic tessellations can have 8-, 10-, and 12-fold rotational symmetries.[16−19] Subwavelength hole arrays can generate SPPs in the terahertz regime through long-range interactions within the quasiperiodic structures, where the number of resonances was higher than periodic PCs.[20] Other work has shown that quasiperiodic tessellated PCs can support SPPs at visible wavelengths.[21−23] The local order around individual nanoholes was found to contribute to the transmission and SPP resonance shape.[22] Because quasiperiodic nanohole arrays are usually fabricated using focused ion beam (FIB) milling, their patterned areas tend to be small (<1 mm^2), which is one reason that only normal incidence measurements have been reported. Other fundamental characteristics of quasiperiodic PCs, such as lifted degeneracies and interactions between modes, have not yet been explored because the investigation of these properties requires larger patterned areas.

Recently, we developed moiré nanolithography, a nanofabrication technique that can produce patterns with rotational symmetries as high as 36-fold over wafer-scale areas.[24] Here we show that these moiré

* Address correspondence to todom@northwestern.edu.

Received for review September 7, 2013 and accepted November 9, 2013.

Published online November 09, 2013
10.1021/nn404703z

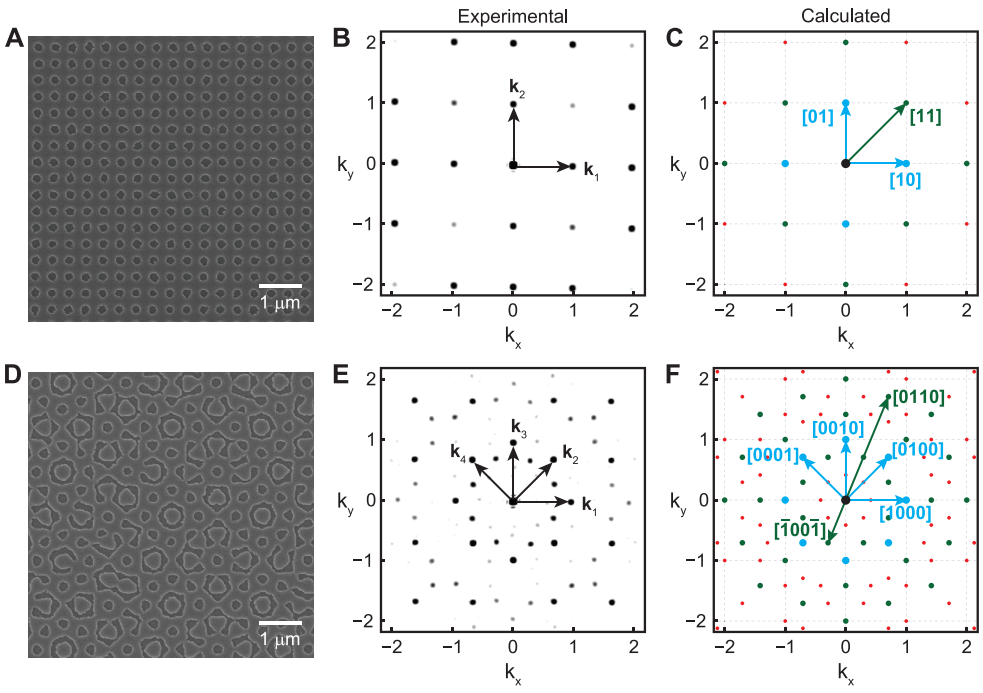

Figure 1. Periodic and moiré plasmonic crystals: (A) SEM image of the Si template for a 4-fold PC; (B) experimental Fourier transform of a square lattice with basis vectors from (A); (C) reciprocal space with indexed reciprocal vectors of a 4-fold lattice; (D) Si template for an 8-fold moiré PC; (E) experimental Fourier transform of an 8-fold lattice; (F) reciprocal space with indexed reciprocal vectors of 8-fold lattice. In (B), (C), (E), and (F), the k_x and k_y axes are in units of $2\pi/a_0$. In (C) and (F), the blue points represent first-order scattering modes, the green points second-order scattering modes, and the red points third-order scattering modes.

nanopatterns, in contrast to moiré PCs limited to periodic geometries,[25,26] can be transferred into plasmonic materials to create quasiperiodic moiré PCs. We measured reflectance spectra of a representative quasiperiodic moiré PC—an 8-fold silver PC—out to high excitation angles. In the form of a dispersion diagram, the angle-resolved data revealed a rich collection of SPP resonances and band gaps. To interpret these features, we developed an indexing system based on the reciprocal lattice vectors of the moiré PCs. This model revealed that the formation of plasmonic band gaps from intersecting SPP modes occurred along Bragg lines at the edges of pseudo-Brillouin zones. Finally, we demonstrated that the plasmonic properties of a moiré PC with an incommensurate 8-fold lattice could also be explained by our new SPP indexing system.

RESULTS AND DISCUSSION

To understand the properties of quasiperiodic moiré PCs, we compared them to periodic PCs. Periodic (4-fold) PCs were fabricated by phase-shifting photolithography using a composite poly(dimethylsiloxane) (PDMS) elastomer mask patterned with a 2D square array of posts on a 400-nm pitch (a_0).[27,28] After a single UV exposure and development, a photoresist (Shipley 1805) pattern of 150-nm diameter features with the same periodicity as the mask was produced over an area of ~5 cm × 5 cm on Si. A Cr layer was deposited followed by lift-off of the photoresist. The Cr film functioned as an etch mask for patterning into Si, where the Si substrate was etched anisotropically using deep reactive ion etching (C_4F_8/SF_6 co-flow). We etched down to 40 nm since this depth has shown efficient plasmonic coupling in gratings.[29,30] The Cr layer was then removed by wet chemical etching to reveal a patterned Si substrate (Figure 1A). Finally, we deposited 160 nm of Ag (optically opaque) on the Si template to create PCs.

In this paper, we describe PCs by their reciprocal lattices generated by the Fourier transform of real-space scanning electron microscopy (SEM) images (Figure 1B). We used a model similar to the empty lattice approximation of free electrons in a crystal lattice to determine the dispersive behavior of individual SPP modes and the band gaps that formed at their intersections.[31] In the Bragg coupling condition, the wavevector of the SPP mode, $\mathbf{k}_{SPP}$, is given by the in-plane wavevector of the incident light, $\mathbf{k}_{||}$, and the grating vector $\mathbf{G}$

$$\mathbf{k}_{SPP} = \mathbf{k}_{||} + \mathbf{G} \quad (1)$$

where $\mathbf{G}$ is defined by

$$\mathbf{G} = \frac{2\pi}{a_0}\mathbf{k} \quad (2)$$

For square lattices, $\mathbf{k} = c_1\mathbf{k}_1 + c_2\mathbf{k}_2$, the linear combination of $\mathbf{k}_1$ and $\mathbf{k}_2$ basis vectors. The constants c_1 and c_2

are integers that define a specific reciprocal vector [c_1 c_2] that corresponds to specific SPP modes on the PC. The scattering order of an SPP mode is defined by the sum of the absolute values of these constants.[2,32] Figure 1C shows the locations of reciprocal vectors that represent the first three SPP scattering orders, where the first order (**G**′) is blue, the second order (**G**″) is green, and the third order (**G**‴) is red.

Through moiré nanolithography, the rotational symmetry of the resulting photoresist pattern can be increased beyond that of the phase-shifting PDMS mask.[24] Three geometric rules govern the fabrication of high-symmetry *n*-fold lattices generated from multiple UV exposures offset by different angles. First, *n* must be an integer multiple of the symmetry of the phase-shifting mask, *n*′. Second, the angular offset between exposures must be equal to 360°/*n*. Third, the number of exposures at equiangular offsets must be equal to *n*/*n*′.[24] Figure 1D shows an 8-fold moiré pattern (*n* = 8) produced from exposing a square phase-shifting mask (*n*′ = 4) twice at an angular offset of 45° (360°/8).

Four basis vectors ($\mathbf{k}_1$, $\mathbf{k}_2$, $\mathbf{k}_3$, and $\mathbf{k}_4$) are present in the 2D Fourier transform of the moiré PC since each square pattern contributes two basis vectors (Figure 1E). As a result, the 8-fold lattice requires more reciprocal vectors to define the lattice compared to the 4-fold case (Figure 1F). For an 8-fold moiré PC, $\mathbf{k} = c_1\mathbf{k}_1 + c_2\mathbf{k}_2 + c_3\mathbf{k}_3 + c_4\mathbf{k}_4$, where c_1, c_2, c_3, and c_4 are integers. By defining four basis vectors, the scattering order of each mode [c_1 c_2 c_3 c_4] can be determined from the sum of the absolute values of each constant, analogous to the 4-fold PCs. Notably, the reciprocal lattice vectors of quasiperiodic structures can exhibit characteristics different from periodic arrays. For example, the vector magnitudes of higher-order reciprocal vectors can be less than those of lower-order ones.[33] In Figure 1F, [$\bar{1}00\bar{1}$] is a second-order reciprocal vector; however, its magnitude is less than that of the first-order [1000] family. This property of quasiperiodic lattices leads to a denser concentration of reciprocal vectors.

Angle-resolved reflectance spectroscopy revealed the propagation of SPP modes associated with the square (4-fold) and 8-fold lattices (Figure 2). Dispersion diagrams were constructed by stitching together a series of angle-resolved spectra and then converting them to energy and in-plane momentum to depict the band structures of the PCs. Figure 2A shows SPP modes on a 4-fold PC at the Ag/air interface, where dips in intensity of the reflected light indicate the excitation of plasmon modes. A sharp SPP mode labeled **I** is clearly seen between 1.6 and 2.5 eV. Above 2.5 eV, specific SPP modes are difficult to identify. Figure 2B shows the calculated SPP modes based on the Bragg coupling condition using the permittivities of Ag[34] where **I** can be clearly identified as the [$\bar{1}$0] mode. The higher-

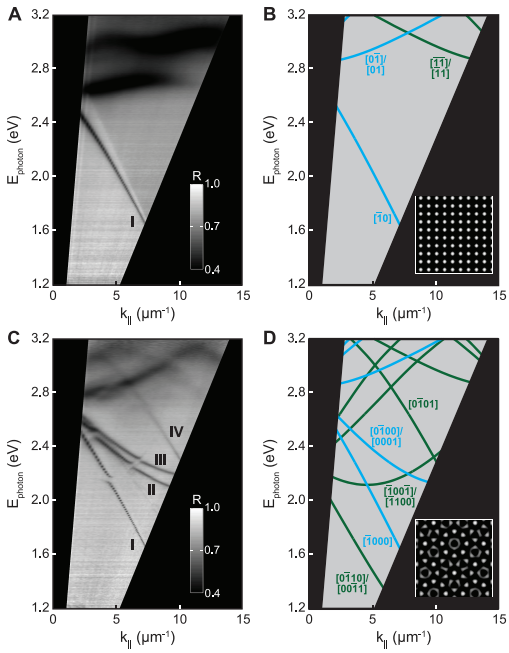

Figure 2. Dispersion diagrams of SPP modes of periodic and moiré plasmonic crystals: (A) experimental dispersion diagrams of a 4-fold PC; (B) calculated dispersion diagram of a square PC with labeled SPP modes; (C) experimental dispersion diagram of an 8-fold moiré PC, where modes of interest are labeled as I, II, III, and IV; (D) calculated dispersion diagram of an 8-fold moiré PC. The calculated dispersion diagrams in (B) and (D) are at the Ag/air interface with a_0 = 400 nm. The blue lines represent first-order modes, and the green lines represent second-order modes.

energy modes are a combination of [0$\bar{1}$], [01], [$\bar{1}\bar{1}$], and [$\bar{1}$1] modes.

Besides the shared modes with the 4-fold PC, the 8-fold moiré PC supported plasmonic band gaps as well as additional SPP modes (Figure 2C). **I** still appeared between 1.6 and 2.5 eV; however, a band gap was present at 2.1 eV. Although the Bragg coupling condition is typically used to identify SPP modes in periodic PCs,[4,9,35] it has not been considered for PCs with higher rotational symmetries. We found that the Bragg model can accurately predict the dispersion of SPP modes in quasiperiodic arrays when the moiré lattice is modeled as a combination of periodic lattices at angular offsets. For an 8-fold moiré lattice, **I** can be identified as the [$\bar{1}$000] mode, analogous with the [$\bar{1}$0] mode in the 4-fold PC (Figure 2D). They are represented by the same **G** vector, which has a magnitude of $2\pi/a_0$ in the $-k_x$ direction. The two new modes that do not have analogous counterparts in the periodic lattice, **II** and **III**, appear between 2.1 and 2.6 eV with band gaps of approximately 0.03 at 2.3 eV. We represent them as [0$\bar{1}$00] and [0001] modes, and they are related to first-order reciprocal vectors that do not exist in the periodic case. The Bragg model predicts that these modes should be degenerate; however, a split between the modes is clearly observed. Azimuthal-angle resolved measurements show that this splitting

is inherent to the higher symmetry lattice (Supporting Information). A weaker mode, **IV**, is also present for this lattice from 2.3 to 3.2 eV. This mode can be assigned as $[0\bar{1}01]$, which is a second-order mode composed of two basis vectors not present in the 4-fold PC.

Plasmonic band gaps can form between intersecting SPP modes along boundaries between adjacent Brillouin zones, similar to how energy gaps form *via* Bragg reflections in electronic band structure.[31,36] Successive Brillouin zones are separated from each other by Bragg lines, which are perpendicular bisectors of their reciprocal-lattice vectors. In the case of Brillouin zones of periodic lattices, certain properties always hold; for example, the individual areas of the zones are equal to each other, and lower-order zones are completely contained within higher-order zones. For structures with higher rotational symmetry, such as our 8-fold moiré PCs, Brillouin zones do not meet these conditions. Instead, here we consider pseudo-Brillouin zones,[37] regions in reciprocal space separated from each other by Bragg lines. We consider these lines as perpendicular bisectors of reciprocal vectors and use them to predict the presence of band gaps at the intersections of SPP modes.

The dispersion diagram in Figure 3A shows the calculated SPP modes of an 8-fold moiré PC. The circled region near 2.1 eV highlights the crossing between the $[\bar{1}000]$ mode and two degenerate second-order modes, $[\bar{1}00\bar{1}]/[\bar{1}100]$. To visualize the interaction between these particular modes in reciprocal space, **G**, $\mathbf{k}_{\|}$, and $\mathbf{k}_{SPP}$ are plotted in Figure 3B. According to the Bragg model, the vector sum of $\mathbf{G}'$ (blue arrow) or $\mathbf{G}''$ (green arrow) and $\mathbf{k}_{\|}$ (orange arrow) is $\mathbf{k}_{SPP}$ (black arrow). Two important properties are seen, which are true for the reciprocal-space representation of any crossing between modes. First, the magnitudes of all of the $\mathbf{k}_{SPP}$ vectors are equal. Second, each $\mathbf{k}_{SPP}$ terminates on Bragg lines of equivalent orders. In this scenario, they each terminate on first-order Bragg lines (dashed blue lines).

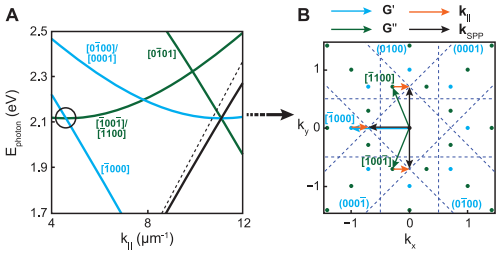

Figure 3. Interactions in reciprocal space of intersecting SPP modes: (A) dispersion diagram for an 8-fold moiré PC at the Ag/air interface (a_0 = 400 nm) showing the first-order (blue) and second-order (green) SPP modes; (B) reciprocal space showing the vectors in the circled region in (A). The k_x and k_y axes are in units of $2\pi/a_0$.

Figure 4A shows an expanded region of the dispersion diagram in Figure 2C with three highlighted intersections, **I**, $\mathbf{II_A}$, and $\mathbf{II_B}$. **I** exhibits a band gap through the $[\bar{1}000]$ mode at the intersection between the two degenerate second-order modes, $[\bar{1}00\bar{1}]/[\bar{1}100]$. $\mathbf{II_A}$ shows the formation of band gaps along the [0001] mode, which is formed at intersections of the second-order modes with the third-order mode $[10\bar{1}1]$ (not shown). Noticeably, there were no band gaps within $\mathbf{II_B}$ even though the [0001] mode intersected the $[\bar{1}00\bar{1}]$ mode in this region. Although a crossing between SPP modes is necessary for the formation of band gaps in these high-symmetry moiré PCs, an intersection alone is not sufficient, and additional conditions must also be met.

Figure 4B shows interactions in reciprocal space for the three areas highlighted in Figure 4A. For the band gap in **I** ($k_{\|}$ = 4.5 μm^{-1}, E = 2.15 eV), the $[\bar{1}000]$ mode crosses the $[\bar{1}00\bar{1}]$ and $[\bar{1}100]$ modes along first-order Bragg lines (bolded diagonal blue lines) (0001), $(0\bar{1}00)$, $(\bar{1}000)$, and (0100). For the region $\mathbf{II_A}$ ($k_{\|}$ = 6.2 μm^{-1}, E = 2.25 eV), the first-order mode [0001] crosses the third-order mode $[10\bar{1}1]$. In reciprocal space, these interactions occur at two Bragg lines in the second-order [1010] family: $(\bar{1}010)$ and $(10\bar{1}0)$ (bolded diagonal green dotted lines). Band gaps can still be formed along these second-order Bragg lines. When the intersections between SPP modes occurred at Bragg lines

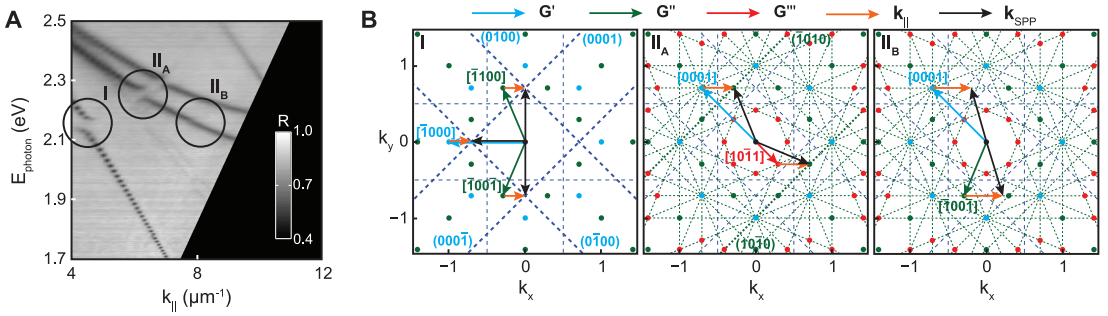

Figure 4. Formation of band gaps in an 8-fold moiré PC: (A) experimental dispersion diagram with three highlighted regions of interest, I, $\mathbf{II_A}$, and $\mathbf{II_B}$; (B) reciprocal space of the three highlighted regions in (A). The vectors in I terminate at first-order Bragg lines; the vectors in $\mathbf{II_A}$ terminate at second-order Bragg lines; the vectors in $\mathbf{II_B}$ do not terminate on a first-order or second-order Bragg line. Band gaps are formed at I and $\mathbf{II_A}$. The k_x and k_y axes are in units of $2\pi/a_0$.

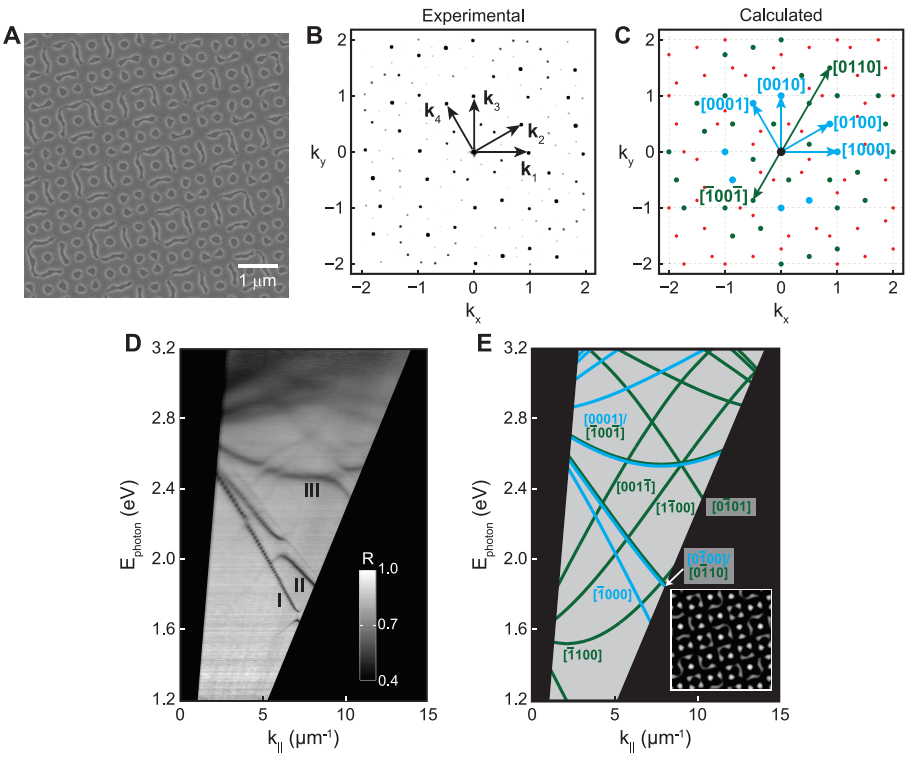

Figure 5. An incommensurate moiré PC: (A) SEM image of the Si template for an incommensurate 8-fold moiré PC; (B) experimental Fourier transform with basis vectors; (C) reciprocal space with indexed reciprocal vectors; (D) experimental dispersion diagram; (E) calculated dispersion diagram.

that were third order or greater, however, band gaps were not observed, as in region **II**$_{\mathbf{B}}$ ($k_{||}$ = 8.0 μm^{-1}, E = 2.16 eV). Similar to **I**, the intersections occurred between a first-order mode [0001] and a second-order mode [$\bar{1}00\bar{1}$]; however, the Bragg lines at which these modes terminate are third order (not shown), and band gaps were not observed. We only highlighted three specific examples; however, our model applies to other intersections in the dispersion diagram as well.

The linear combinations of basis vectors that define reciprocal vectors and pseudo-Brillouin zones are not limited to quasiperiodic PCs with high rotational symmetries. Quasiperiodic moiré PCs can also be created with geometries that do not exceed the rotational symmetries of their constituent phase-shifting PDMS masks. We classify these structures as incommensurate since their rotational symmetries are within the crystallographic restriction theorem.[15] Although the symmetry has not increased, these PCs still display properties similar to their quasiperiodic counterparts. For example, an incommensurate moiré PC can be created by exposing twice through 2D square array PDMS masks at 30° instead of 45° (Figure 5A). These conditions do not satisfy the geometric rules discussed earlier for the creation of higher symmetry lattices; hence, the overall rotational symmetry of this modified lattice is only 4-fold. Four basis vectors can still be defined (labeled $\mathbf{k}_1$, $\mathbf{k}_2$, $\mathbf{k}_3$, and $\mathbf{k}_4$), but they are not equiangular (Figure 5B). Alternatively, we could have indexed this system as a 4-fold lattice with a two-unit basis. As with 8-fold moiré PCs, the scattering order of the SPP modes [c_1 c_2 c_3 c_4] can be determined from the sum of the absolute values of the constants. Specific reciprocal vectors are indexed as linear combinations of the four basis vectors in Figure 5C.

In the incommensurate lattice, fewer SPP modes are degenerate compared to the 8-fold case since the overall symmetry is lower. As a result, more intersections between SPP modes occur and more band gaps are observed (Figure 5D). Similar to the 8-fold case, four basis vectors were used to index the SPP modes, although different angles for the $\mathbf{k}_2$ (30° instead of 45°) and $\mathbf{k}_4$ (120° instead of 135°) basis vectors reflect the new geometry (Figure 5E). As with the periodic 4-fold PC and 8-fold moiré PC, **I** is the [$\bar{1}$000] mode between the energies of 1.6 and 2.5 eV. A band gap at 1.7 eV is present along this mode, which was absent in the 8-fold moiré PC. **II** is the [0$\bar{1}$00] mode between the energies of 1.8 and 2.5 eV. This mode has a prominent band gap at 2.1 eV. Additionally, a weaker SPP mode [0$\bar{1}$10] appears near this mode at higher energies. The Bragg model predicts these two modes to be degenerate, but we observe a splitting in energy because of a slight misalignment of the azimuthal angle (≈1°) of the substrate during the measurements. **III** consists of the [0001]/[$\bar{1}00\bar{1}$] modes between 2.5 and 2.7 eV, which contain several band gaps.

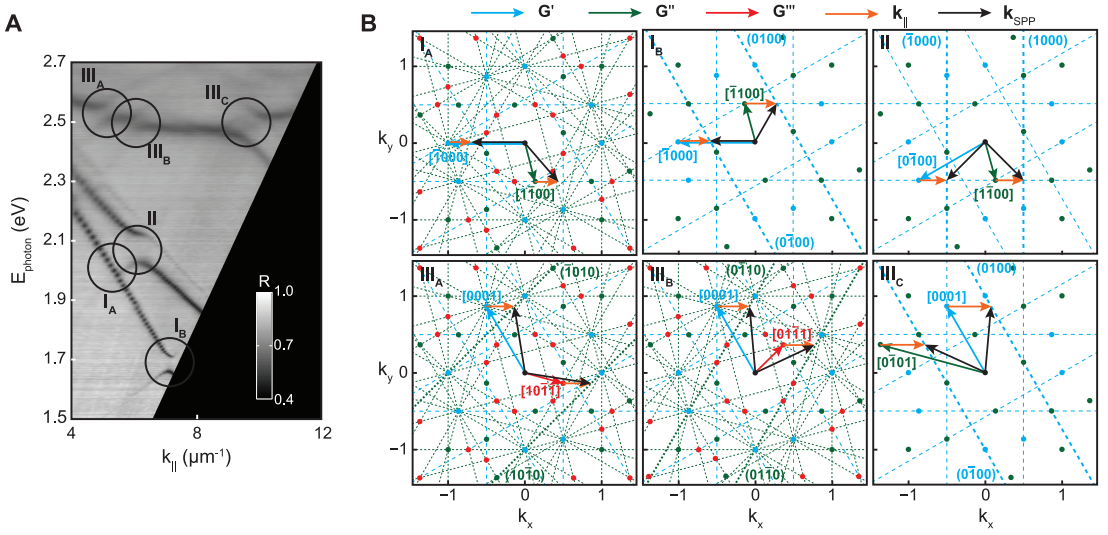

Figure 6. Formation of band gaps in an incommensurate 8-fold moiré PC: (A) experimental dispersion diagram with six highlighted regions of interest, I_A, I_B, II, III_A, III_B, and III_C; (B) reciprocal space of the regions in (A). The vectors in I_B, II, and III_C all terminate at first-order Bragg lines; the vectors in III_A and III_B terminate at second-order Bragg lines; the vectors in I_A do not terminate on a first-order or second-order Bragg line. Band gaps are formed at I_B, II, III_A, III_B, and III_C. The k_x and k_y axes are in units of $2\pi/a_0$.

To analyze the band gaps in the incommensurate moiré PC, we zoomed in on an area and highlighted six regions with black circles (Figure 6A). Similar to the 8-fold case in Figure 4, Bragg lines can be used to determine the location and presence of band gaps along SPP modes. Figure 6B shows interactions in reciprocal space for the six areas of interest. The $[\bar{1}000]$ and $[1\bar{1}00]$ modes cross in the $\mathbf{I_A}$ ($k_{||} = 5.2\ \mu m^{-1}$, $E = 2.00$ eV) region; the Bragg line at which each $\mathbf{k_{SPP}}$ terminates is third order (not shown), and no band gap was formed. For regions $\mathbf{I_B}$, **II**, and $\mathbf{III_C}$, band gaps were formed at the intersections between first-order and second-order modes and along first-order Bragg lines. The $[\bar{1}000]$ mode terminates at the $(0\bar{1}00)$ line and the $[\bar{1}100]$ mode terminates at the (0100) line for $\mathbf{I_B}$ ($k_{||} = 7.1\ \mu m^{-1}$, $E = 1.68$ eV); the $[0\bar{1}00]$ mode terminates at the $(\bar{1}000)$ line and the $[1\bar{1}00]$ mode terminates at the (1000) line for **II** ($k_{||} = 6.1\ \mu m^{-1}$, $E = 2.06$ eV), and the [0001] mode terminates at the (0100) line and the $[0\bar{1}01]$ mode terminates at the $(0\bar{1}00)$ line for $\mathbf{III_C}$ ($k_{||} = 9.7\ \mu m^{-1}$, $E = 2.52$ eV). For the $\mathbf{III_A}$ and $\mathbf{III_B}$ regions, band gaps were formed at the intersection between first-order and third-order modes along second-order Bragg lines. The [0001] and $[100\bar{1}]$ modes terminated at the $(\bar{1}010)/(10\bar{1}0)$ Bragg lines for $\mathbf{III_A}$ ($k_{||} = 5.1\ \mu m^{-1}$, $E = 2.54$ eV), and the [0001] and $[01\bar{1}1]$ modes terminated at the $(0\bar{1}10)/(01\bar{1}0)$ Bragg lines for $\mathbf{III_B}$ ($k_{||} = 6.0\ \mu m^{-1}$, $E = 2.52$ eV). The same general rules apply to this incommensurate PC as with the 8-fold structure. Band gaps form if the SPP modes intersected along a first-order or second-order Bragg line at the boundary of a pseudo-Brillouin zone; however, they did not form at higher-order Bragg lines.

CONCLUSIONS

In summary, we have demonstrated that quasiperiodic moiré PCs show rich SPP dispersion diagrams. We observed an increase in the number of SPP modes compared to periodic PCs as well as the presence of plasmonic band gaps that formed at certain intersections. By adapting the Bragg model, we created an indexing system that could predict and explain the behavior of SPP modes. Additionally, by defining pseudo-Brillouin zones and Bragg lines in these quasiperiodic arrays, we could determine the location of plasmonic band gaps. This model is versatile and can be applied to any plasmonic substrate with quasiperiodic symmetry. Since quasiperiodic moiré PCs can trap light over a broadband visible spectrum and generate tunable band gaps, we anticipate that they will expand possibilities of plasmonic devices that currently exploit periodic PCs.

METHODS

Phase-Shifting Photolithography and Moiré Nanolithography. A PDMS photomask with a square lattice spacing of 400 nm was placed into conformal contact with diluted, positive-tone, g-line photoresist (PR) (Shipley S1805; ~120 nm thick) on a Si (100) wafer and exposed to a broadband Hg-vapor light source (SUSS MicroTec MA6) at a power density of 11 mW/cm^2. The mask was exposed for 1.5 s to create the square pattern and exposed twice at 0.6 s for the moiré patterns. The mask was offset by 45° between exposures to create the 8-fold lattice and 30° to create the incommensurate lattice. The exposed PR was developed (1:5 dilution of Microposit 351 developer) and resulted in arrays of PR posts on a Si substrate.

Pattern Transfer. To remove residual PR, the samples were exposed to an O_2 plasma. A 14-nm Cr sacrificial layer was

deposited onto the substrate with a Kurt J. Lesker PVD-75 Electron Beam Deposition System. The PR posts were removed using Microposit Remover 1165 leaving circular holes in the Cr layer. Si wells with depths of 40 nm were anisotropically etched using a C_4F_8/SF_6 co-flow recipe with a STS LpX Pegasus Deep Reactive Ion Etcher. The Cr layer was removed, and 160 nm of Ag was deposited in the PVD-75 onto the Si grating to create the plasmonic crystals.

Angle-Resolved Reflectance Spectroscopy. Zero-order reflectance spectra were collected from $\theta = 10°$ to 60° in 1° increments using an automated, self-designed National Instruments LabVIEW program. Collimated, unpolarized white light from a halogen lamp (100 W) illuminated the sample with a spot size of 2 mm. The reflected light was coupled into a bundled optical fiber connected to a Princeton Instruments Acton SP2500 spectrometer with a PIXIS:400 CCD detector. A linear interpolation algorithm in Matlab converted the measured optical data (wavelength (λ) and excitation angle (θ)) into dispersion diagrams (photon energy (E_{photon}) and in-plane wavevector of light ($\mathbf{k}_{||}$)) using the following: $E_{photon} = hc/\lambda$ and $\mathbf{k}_{||} = (2\pi/\lambda) \sin\theta$.

Conflict of Interest: The authors declare no competing financial interest.

Acknowledgment. This work was supported by the National Science Foundation (NSF) under NSF Award Numbers DMR-1006380 and CMMI-1069180 (S.M.L., T.W.O.). We acknowledge government support under FA9550-05-C-0059 (M.D.H.) and FA9550-11-C-0028 (A.J.H.) awarded by DoD, Air Force Office of Scientific Research, National Defense Science and Engineering Graduate (NDSEG) Fellowship, 32 CFR 168a. This work made use of the NUANCE Center facilities, which are supported by NSF-MRSEC, NSF-NSC, the Keck Foundation, and the Materials Processing and Microfabrication Facility, which is supported by the MRSEC program of the NSF (DMR-1121262).

Supporting Information Available: Dispersion diagram equations; explanation of calculated degeneracies; reciprocal-lattice schemes with indexed reciprocal vectors for square, 8-fold, and incommensurate arrays; reciprocal-lattice schemes with indexed Bragg lines for square, 8-fold, and incommensurate 8-fold arrays; azimuthal-angle resolved reflectance spectroscopy of square and 8-fold PCs. This material is available free of charge *via* the Internet at http://pubs.acs.org.

REFERENCES AND NOTES

1. Genet, C.; Ebbesen, T. W. Light in Tiny Holes. *Nature* **2007**, *445*, 39–46.
2. Barnes, W. L.; Dereux, A.; Ebbesen, T. W. Surface Plasmon Subwavelength Optics. *Nature* **2003**, *424*, 824–830.
3. Raether, H. Surface-Plasmons on Smooth and Rough Surfaces and on Gratings. *Springer Tracts Mod. Phys.* **1988**, *111*, 1–133.
4. Barnes, W. L.; Preist, T. W.; Kitson, S. C.; Sambles, J. R.; Cotter, N. P. K.; Nash, D. J. Photonic Gaps in the Dispersion of Surface-Plasmons on Gratings. *Phys. Rev. B* **1995**, *51*, 11164–11167.
5. Gao, H. W.; Zhou, W.; Odom, T. W. Plasmonic Crystals: A Platform to Catalog Resonances from Ultraviolet to Near-Infrared Wavelengths in a Plasmonic Library. *Adv. Funct. Mater.* **2010**, *20*, 529–539.
6. Maier, S. A. *Plasmonics: Fundamentals and Applications*: Springer: New York, 2007.
7. Stewart, M. E.; Mack, N. H.; Malyarchuk, V.; Soares, J. A. N. T.; Lee, T. W.; Gray, S. K.; Nuzzo, R. G.; Rogers, J. A. Quantitative Multispectral Biosensing and 1D Imaging using Quasi-3D Plasmonic Crystals. *Proc. Natl. Acad. Sci. U.S.A.* **2006**, *103*, 17143–17148.
8. Lin, J. Y.; Stuparu, A. D.; Huntington, M. D.; Mrksich, M.; Odom, T. W. Nanopatterned Substrates Increase Surface Sensitivity for Real-Time Biosensing. *J. Phys. Chem. C* **2013**, *117*, 5286–5292.
9. Ebbesen, T. W.; Lezec, H. J.; Ghaemi, H. F.; Thio, T.; Wolff, P. A. Extraordinary Optical Transmission through Sub-Wavelength Hole Arrays. *Nature* **1998**, *391*, 667–669.
10. Gao, H. W.; Hyun, J. K.; Lee, M. H.; Yang, J. C.; Lauhon, L. J.; Odom, T. W. Broadband Plasmonic Microlenses Based on Patches of Nanoholes. *Nano Lett.* **2010**, *10*, 4111–4116.
11. Atwater, H. A.; Polman, A. Plasmonics for Improved Photovoltaic Devices. *Nat. Mater.* **2010**, *9*, 205–213.
12. Odom, T. W.; Gao, H. W.; McMahon, J. M.; Henzie, J.; Schatz, G. C. Plasmonic Superlattices: Hierarchical Subwavelength Hole Arrays. *Chem. Phys. Lett.* **2009**, *483*, 187–192.
13. Zhou, W.; Gao, H. W.; Odom, T. W. Toward Broadband Plasmonics: Tuning Dispersion in Rhombic Plasmonic Crystals. *ACS Nano* **2010**, *4*, 1241–1247.
14. Hiller, H. The Crystallographic Restriction in Higher Dimensions. *Acta Crystallogr., Sect. A* **1985**, *41*, 541–544.
15. Steinhardt, P. J.; Ostlund, S. *The Physics of Quasicrystals*; World Scientific: Teaneck, NJ, 1987; p xvi, 767.
16. Harriss, E. O.; Lamb, J. S. W. Canonical Substitutions Tilings of Ammann-Beenker Type. *Theor. Comput. Sci.* **2004**, *319*, 241–279.
17. Ammann, R.; Grünbaum, B.; Shephard, G. Aperiodic Tiles. *Discrete Comput. Geom.* **1992**, *8*, 1–25.
18. Penrose, R. The Role of Aesthetics in Pure and Applied Mathematical Research. *Bull. Inst. Math. Appl.* **1974**, *10*, 266–271.
19. Socolar, J. E. S. Simple Octagonal and Dodecagonal Quasicrystals. *Phys. Rev. B* **1989**, *39*, 10519–10551.
20. Matsui, T.; Agrawal, A.; Nahata, A.; Vardeny, Z. V. Transmission Resonances through Aperiodic Arrays of Subwavelength Apertures. *Nature* **2007**, *446*, 517–521.
21. Przybilla, F.; Genet, C.; Ebbesen, T. W. Enhanced Transmission through Penrose Subwavelength Hole Arrays. *Appl. Phys. Lett.* **2006**, *89*, 121115.
22. Pacifici, D.; Lezec, H. J.; Sweatlock, L. A.; Walters, R. J.; Atwater, H. A. Universal Optical Transmission Features in Periodic and Quasiperiodic Hole Arrays. *Opt. Express* **2008**, *16*, 9222–9238.
23. Xue, J.; Zhou, W. Z.; Dong, B. Q.; Wang, X.; Chen, Y. F.; Huq, E.; Zeng, W.; Qu, X. P.; Liu, R. Surface Plasmon Enhanced Transmission through Planar Gold Quasicrystals Fabricated by Focused Ion Beam Technique. *Microelectron. Eng.* **2009**, *86*, 1131–1133.
24. Lubin, S. M.; Zhou, W.; Hryn, A. J.; Huntington, M. D.; Odom, T. W. High-Rotational Symmetry Lattices Fabricated by Moiré Nanolithography. *Nano Lett.* **2012**, *12*, 4948–4952.
25. Balci, S.; Kocabas, A.; Kocabas, C.; Aydinli, A. Localization of Surface Plasmon Polaritons in Hexagonal Arrays of Moire Cavities. *Appl. Phys. Lett.* **2011**, *98*, 031101.
26. Balci, S.; Karabiyik, M.; Kocabas, A.; Kocabas, C.; Aydinli, A. Coupled Plasmonic Cavities on Moire Surfaces. *Plasmonics* **2010**, *5*, 429–436.
27. Rogers, J. A.; Paul, K. E.; Jackman, R. J.; Whitesides, G. M. Using an Elastomeric Phase Mask for Sub-100 nm Photolithography in the Optical Near Field. *Appl. Phys. Lett.* **1997**, *70*, 2658–2660.
28. Rogers, J. A.; Paul, K. E.; Jackman, R. J.; Whitesides, G. M. Generating ~90 Nanometer Features Using Near-Field Contact-Mode Photolithography with an Elastomeric Phase Mask. *J. Vac. Sci. Technol., B* **1998**, *16*, 59–68.
29. Hall, A. S.; Friesen, S. A.; Mallouk, T. E. Wafer-Scale Fabrication of Plasmonic Crystals from Patterned Silicon Templates Prepared by Nanosphere Lithography. *Nano Lett.* **2013**, *13*, 2623–2627.
30. MacDonald, K. F.; Samson, Z. L.; Stockman, M. I.; Zheludev, N. I. Ultrafast Active Plasmonics. *Nat. Photonics* **2009**, *3*, 55–58.
31. Kittel, C. *Introduction to Solid State Physics*, 8th ed.; Wiley: Hoboken, NJ, 2005; pp xix, 680.
32. Martin-Moreno, L.; Garcia-Vidal, F. J.; Lezec, H. J.; Pellerin, K. M.; Thio, T.; Pendry, J. B.; Ebbesen, T. W. Theory of Extraordinary Optical Transmission through Subwavelength Hole Arrays. *Phys. Rev. Lett.* **2001**, *86*, 1114–1117.
33. Levine, D.; Steinhardt, P. J. Quasicrystals—A New Class of Ordered Structures. *Phys. Rev. Lett.* **1984**, *53*, 2477–2480.
34. Johnson, P. B.; Christy, R. W. Optical Constants of Noble Metals. *Phys. Rev. B* **1972**, *6*, 4370–4379.

35. Barnes, W. L.; Preist, T. W.; Kitson, S. C.; Sambles, J. R. Physical Origin of Photonic Energy Gaps in the Propagation of Surface Plasmons on Gratings. *Phys. Rev. B* **1996**, *54*, 6227–6244.
36. Ashcroft, N. W.; Mermin, N. D. *Solid State Physics*; Brooks/Cole: Pacific Grove, CA, 1976; pp xxi, 826.
37. Janssen, T. Quasicrystals: Comparative Dynamics. *Nat. Mater.* **2007**, *6*, 925–926.